Geophysical Journal International

*Geophys. J. Int.* (2025) **243,** 1–11
Advance Access publication 2025 August 13
Research Paper

https://doi.org/10.1093/gji/ggaf315

# Broad-band spectral electrical impedance tomography (sEIT) measurements with a centralized multiplexer and coaxial cables

Haoran Che [1,2] Johan Alexander Huisman[1] and Egon Zimmermann[3]

[1] *Agrosphere (IBG-3), Institute of Bio- and Geosciences, Forschungszentrum Jülich GmbH, 52428, Jülich, Germany*
[2] *Division of Engineering Geology, Lund University, 22100 Lund, Sweden . E-mail: haoran.che@tg.lth.se*
[3] *Institute of Technology and Engineering (ITE), Forschungszentrum Jülich GmbH, 52428, Jülich, Germany*

Accepted 2025 August 12. Received 2025 July 16; in original form 2024 December 18

## SUMMARY

Spectral electrical impedance tomography (sEIT) has attracted increasing interest in hydrogeology, biogeosciences, agriculture and environmental studies. However, broad-band sEIT measurements, particularly at frequencies above 50 Hz, have long been challenging due to electromagnetic (EM) coupling effects. Recent advances in instrumentation, data correction and filtering have improved sEIT measurements at higher frequencies, yet many of these developments rely on a customized system with distributed amplifiers. Extending these advancements to more universally applicable methods is necessary, as sEIT measurements are often acquired using systems with centralized multiplexers. This study aims to bridge this gap by developing model-based data correction methods to mitigate EM coupling effects in sEIT measurements acquired with such a set-up. For this, the differences in EM coupling effects between measurements with a centralized multiplexer and distributed amplifiers were discussed, and the required correction methods in case of a centralized multiplexer were developed. The effectiveness of the developed corrections was tested using sEIT measurements acquired with a centralized multiplexer. A data set obtained using distributed amplifiers and corrected using previously developed approaches served as a reference. Finally, inversion results of all data sets were compared. It was shown that cable capacitance dominates the capacitive coupling in the sEIT measurements acquired with a centralized multiplexer when coaxial cables are used. Improvements were observed after each correction step using the developed methods. It was concluded that broad-band sEIT imaging results can be obtained using measurements with a centralized multiplexer and coaxial cables using the proposed data correction and filtering methods.

**Key words:** Electromagnetic theory; Induced polarization; Tomography.

## 1. INTRODUCTION

Spectral electrical impedance tomography (sEIT) is a non-invasive geophysical method to map the subsurface complex electrical conductivity distribution over a broad frequency range from mHz to kHz. While extensive research has demonstrated the value of laboratory spectral induced polarization (SIP) measurements in characterizing microscopic structures and processes in soil, sediment and rocks (Personna *et al.* 2008; Aal & Atekwana 2014; Mellage *et al.* 2018; Izumoto *et al.* 2020), bridging the gap between these promising lab-based results and their practical application in the field remains a significant challenge. In recent years, there have been several attempts in obtaining the distribution of the complex electrical conductivity at the field scale using sEIT, particularly in the case of environmental and hydrogeophysical applications such as contaminated site characterization (Flores-Orozco *et al.* 2012), biogeochemical investigations (Williams *et al.* 2009; Flores Orozco *et al.* 2011) and hydraulic conductivity determination (Attwa & Günther 2013). However, these studies were all focused on the lower frequency range below 50 Hz. Broad-band sEIT measurements are desirable to characterize the full complexity of the electrical response of the investigated materials. Unfortunately, electromagnetic (EM) coupling effects including both inductive and capacitive coupling strongly affect sEIT measurements in the higher frequency range ($>$ 50 Hz), which has long been a crucial problem for broad-band sEIT measurements. To deal with EM coupling effects, full scale modelling and inversion based on Maxwell's equations would be ideal (Commer *et al.* 2011; Qi *et al.* 2019), but it is computationally expensive and complicated to implement. Previous studies addressing these EM coupling effects in sEIT measurements either focused solely on the inductive coupling effect or lumped the inductive and capacitive coupling together (Wait & Gruszka 1986; Routh

& Oldenburg 2001; Schmutz *et al.* 2014; Flores Orozco *et al.* 2021). However, both types of coupling have distinct sources, and should thus preferably be separately addressed.

Inductive coupling in sEIT measurements usually refers to the cable-to-cable effect due to mutual inductance. In particular, alternating current propagating in a wire induces an electromagnetic field, which creates voltage errors in the wires used for potential measurement. For near-surface applications with relatively short cables, the induction effect from the soil can be neglected in the frequency range from mHz to kHz (Wait 1984; Zhao *et al.* 2015). In this case, the inductive coupling mainly depends on the geometry of cables and can be corrected using the mutual inductance. The mutual inductance can be numerically calculated when the geometry and arrangement of measurement cables are known (Zimmermann *et al.* 2019) or can be calibrated in the case of a cable bundle (Zhao *et al.* 2013, 2015; Weigand *et al.* 2022). Wang *et al.* (2021) proposed a novel index to quantify the inductive coupling strength (ICS) for each sEIT measurement. Through ICS-based experimental design, reliable broad-band sEIT inversion results up to kHz were achieved without correction for inductive coupling.

Compared to inductive coupling, capacitive coupling effects are much more complex to address. Depending on the measurement technique, type of cables and the cable arrangements, capacitive coupling affects sEIT measurements in different ways and to a varying degree. It has been shown that the most commonly used multicore cables in geoelectrical measurements have the strongest EM coupling effects due to the millimetre scale distance between the inner conductors (Flores Orozco *et al.* 2021). The small separation between wires results in both strong inductive coupling and significant capacitive coupling effects. Dahlin & Leroux (2012) developed a parallel cable layout in which the current transmission and voltage measurement are carried out in two separated parallel cables. The parallel cable layout perfectly solved problems due to electrode charge-up effects associated with the alternating use of electrodes for current injections and potential measurements. However, the improvement in suppressing EM coupling effects was found to be limited (Flores Orozco *et al.* 2021; Wang *et al.* 2021). With the use of coaxial cables, the capacitive coupling between wires can be eliminated because the potential on the shielding of all cables is the same (i.e. no leakage current between cables). However, the use of coaxial cables introduces a new type of capacitive coupling between the shielding and the inner wire. The shielding of all cables is connected to the system ground, while the inner wires are connected to the electrodes. This setup creates a potential difference between the shielding and the inner wires. This potential difference drives a leakage current that flows between the shielding and the inner wire. This type of capacitive coupling can be greatly reduced by using distributed amplifiers at the electrodes for voltage measurement, as implemented in the sEIT system of Zimmermann *et al.* (2008). Even when distributed amplifiers and coaxial cables are used, there still is capacitive coupling between the subsurface and the cable shield. This type of capacitive coupling can be minimized by lifting the cables in the air (Weigand *et al.* 2022), which is cumbersome and only seems feasible for sEIT measurement set-ups used for long-term monitoring. In cases where the cables have direct contact with the ground surface, this type of capacitive coupling can be corrected by integrating the measured leakage current and total capacitance between subsurface and shield in finite element forward modelling (FEM) (Zimmermann *et al.* 2019). Based on this correction strategy, Wang *et al.* (2024) proposed a data processing and filtering approach to identify electrode configurations that are less affected by this type of capacitive coupling. The advancements reviewed above were all based on a sEIT system with distributed amplifiers, enabling accurate broad-band sEIT measurements and inversion results up to kHz frequencies. However, centralized multiplexers are more commonly used in commercially available EIT systems due to their robustness for cable handling in the field. Distributed amplifiers require more effort to assemble and demand careful handling during deployment. Therefore, it is important to investigate methods for mitigating capacitive coupling effects in centralized multiplexer systems. This would potentially enable more accurate broad-band sEIT results using widely available commercial systems.

The aim of this study is to develop correction methods for capacitive coupling in sEIT measurements when a centralized multiplexer with coaxial cables is used. In the first step, the measurement setups will be described in detail and the difference between distributed amplifiers and a centralized multiplexer in terms of capacitive coupling effects will be illustrated. Next, correction methods and data processing procedures for measurements with both setups will be presented. In the final step, results of sEIT measurements with a centralized multiplexer before and after each developed correction step will be compared with reference data acquired with distributed amplifiers.

## 2. MATERIALS AND METHODS

### 2.1 sEIT measurement system and setups

Acquisition of sEIT measurements relied on a customized system developed by Zimmerman *et al.* (2008) and extended by Zimmermann *et al.* (2010). The customized sEIT system (Fig. 1a) has 40 channels and measures voltage at each electrode relative to the system ground. It also measures currents at the positive ($I_1$) and negative ($I_2$) current channels, allowing the calculation of the leakage current ($I_L = I_1 + I_2$) and the symmetric current ($I_s = 0.5I_1 - 0.5I_2$). The system was designed to use distributed amplifiers for voltage measurement at each electrode (i.e. amplifiers mounted at electrodes), which is referred to as an active setup (Figs 1b and e) in this study. The amplifier module incorporates a relay to switch between current injection and potential measurement modes for each channel. To simulate a centralized multiplexer, a connector hub with 20 amplifier modules was built (Fig. 1c). The connector hub was connected to the system with individual short coaxial cables (1 m). The shielding of all cables was connected to the system ground. This measurement setup with a simulated centralized multiplexer is referred to as a passive setup (Figs 1d and f) in this study. Figs 1(g) and (h) provide a schematic illustration of one channel of the active and passive setup, respectively. It should be noted that the actual passive setup employed in this study includes a 1 m section of the active setup, which simulates the centralized multiplexer as shown in Fig. 1(f). However, to emphasize the general concept of active and passive setups, this short section of the active setup within the passive setup is omitted in Fig. 1(h). The main difference between the active and passive setups is the position of the amplifiers used for voltage measurement. When the relays are switched for current injections, there is no difference between the active and passive setup. A detailed discussion of the capacitive coupling effects in both active and passive setups will be provided after the field data acquisition and the treatment of inductive coupling have been addressed.

Field sEIT measurements with different setups were acquired at the campus of the Forschungszentrum Jülich, Germany

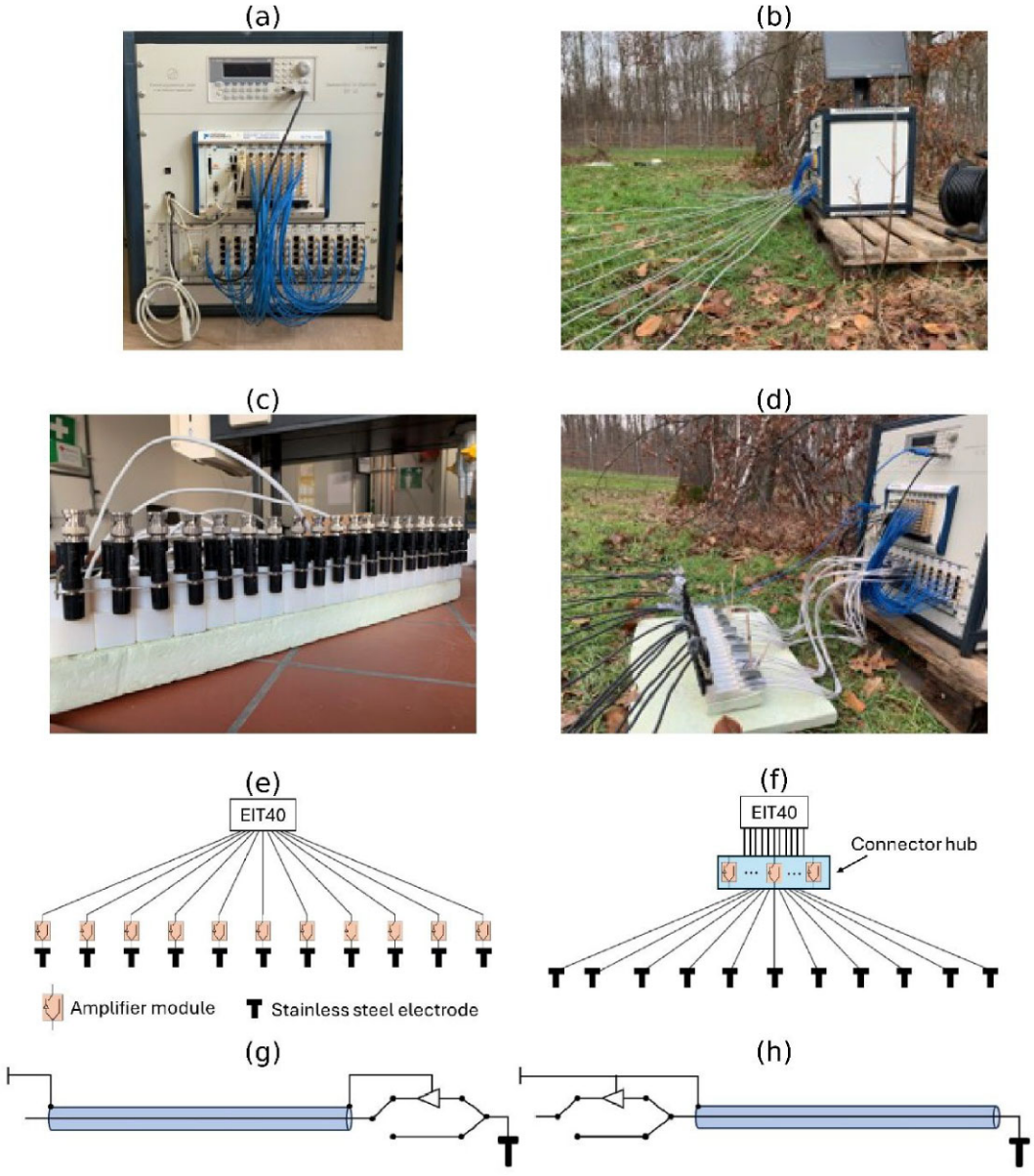


**Figure 1.** (a) sEIT measurement system developed by Zimmermann *et al.* (2008) and extended by Zimmermann *et al.* (2010); (b) illustration of active set-up; (c) connector hub with 20 amplifier modules; (d) illustration of passive set-up; schematic sketches of (e) the full active setup, (f) the full passive setup, one channel of the (g) active setup and (h) passive setup.

(50°54′37.2‘N 6°24′14.6″E). The electrode layout consisted of 11 electrodes with 1 m electrode spacing. The 10 m long cables were arranged in a fan-shaped layout with the system placed 4 m away from the survey line (Zimmermann *et al.* 2019; Wang *et al.* 2024). Since the system measures the potential at each single electrode relative to system ground, only the electrode pairs used for current excitation need to be specified *a priori*. A skip-6 circulating scheme was used for current excitation (Xu & Noel 1993), in which 6 electrodes were skipped between the two current electrodes for each excitation (i.e. current excitation at 01–08, 08–04, 04–11, . . . , 05–01). This results in 11 current injections and 396 four-pole measurements that can be obtained in the post-processing. The measurements were acquired at 12 frequencies, logarithmically distributed over a broad frequency range from 1 Hz to 10 kHz. The set of 396 measurements contains different types of electrode configurations, including Alpha, Beta and Gamma types (Carpenter & Habberjam 1956). To identify configurations with poor data quality, the so-called geometric factor relative error was used (Wilkinson *et al.* 2008; Loke *et al.* 2014). This measure evaluates the relative error in the geometric factor due to a small change in the electrode position. A cut-off factor of 5 ($m^{-1}$) was used in this study, which corresponds to a maximum 5 per cent relative error in the geometric factor for a 1 cm uncertainty in electrode position. After filtering for high relative errors, 378 configurations remained.

### 2.2 Inductive coupling

Inductive coupling in sEIT measurements comprises both cable-to-cable and cable-to-subsurface effects. For short grounded electrode wires, the cable-to-subsurface induction effect can generally be neglected but still depends on the frequency range and

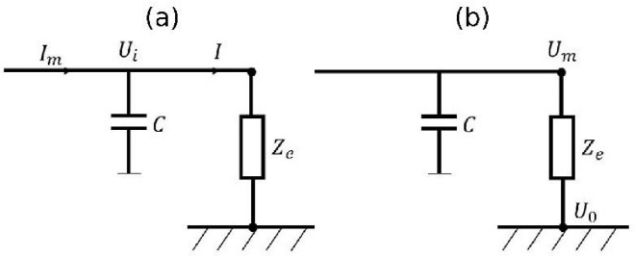


**Figure 2.** Electric circuit models for the (a) current channel and (b) voltage channel. $C$ represents the cable capacitance in both cases.

subsurface conditions. However, this effect should be considered at very high frequencies (over 10 kHz) or with very large array layouts (over 50 m), as encountered in applications like permafrost imaging (Schulz *et al.* 2025). In this study, only the cable-to-cable effect was considered, which mainly depends on the position of the cables in the case of short electrode layouts and can be quantified by the mutual inductance $M$. The mutual inductance $M$ for a given cable layout can be numerically calculated by a Neumann's integral (Sunde 1968; Zhao *et al.* 2013). After calculating the mutual inductance $M$, the inductive coupling can be removed using (Zhao *et al.* 2013):

$$Z^* = Z_m^* - i\omega M, \tag{1}$$

where $\omega$ is the angular frequency, $i$ is the imaginary unit, $Z_m^*$ is the measured complex impedance and $Z^*$ is the complex impedance after correction of inductive coupling. To quantify the strength of inductive coupling, Wang *et al.* (2021) proposed the inductive coupling strength (ICS), which is calculated using:

$$\text{ICS} = 100\,\text{per cent} \times \frac{\omega M}{Z_0''}, \tag{2}$$

where $Z_0''$ is the error-free imaginary part of the complex impedance or the representative signal strength. For experimental design purposes, $Z_0''$ can be calculated analytically assuming a homogeneous subsurface model (Wang *et al.* 2021). In this study, the ICS of all measurements was calculated using the corrected imaginary part of the complex impedance $Z_0''$.

### 2.3 Capacitive coupling effects in the active setup

There are two dominant types of capacitive coupling when using the active setup. One type of coupling is due to the cable capacitance (inner wire to shield) of the current channels. Although the active setup relies on distributed amplifiers at the electrodes, it only prevents the effect of the cable capacitance at the channels for voltage measurements. At the current channels (Fig. 2a), leakage current can flow back to the system through the cable capacitance. As a result, the measured current consists of the current flowing through the electrodes into the soil and the leakage current through the cable capacitance. Since the system also measures the voltage $U_i$ at each single current channel, the true current $I$ flowing through the electrode can be calculated using

$$I = I_m - i\omega C U_i, \tag{3}$$

where $I_m$ is the measured current, and $C$ is the capacitance of the coaxial cable.

After correction of the currents at the positive and negative current channels, the summation of the two currents represents the leakage current through the capacitance between shield and subsurface in the active set-up, which is the other type of capacitive coupling in the active setup. This type of capacitive coupling effect can be modelled and corrected (Zimmermann *et al.* 2019; Wang *et al.* 2024), which requires information on the total capacitance between the shield and the subsurface, the leakage current through the total capacitance and the distribution of the real part of the complex electrical conductivity in the subsurface. The procedure for modelling and correction is as follows. First, the measured real part of the complex impedances is inverted to obtain the distribution of the real part of the electrical conductivity. Next, the obtained 2-D distribution is extended into a 3-D subsurface model, and the measured total capacitance is distributed along the cable. After this, finite element forward modelling using the measured leakage current is used to correct the measured impedances with the modelled imaginary part impedances $Z_{\text{fem}}''$ using:

$$Z^* = Z_m^* - i Z_{\text{fem}}''. \tag{4}$$

The leakage current through the subsurface and shield is mainly driven by the real part of the potential distribution. Therefore, the induced error in the imaginary part of the impedance can be modelled with only the real part of the electrical conductivity distribution. For more details about the FEM-based modelling, we refer to Wang *et al.* (2024).

To evaluate the FEM-based correction, the capacitive coupling strength (CCS) was proposed by Wang *et al.* (2024):

$$\text{CCS} = 100\,\text{per cent} \times \frac{Z_{\text{fem}}''}{Z_0''}. \tag{5}$$

The CCS is defined as the percentage ratio of the modelled imaginary part of the complex impedance due to subsurface-to-shield capacitive coupling and the imaginary part of complex impedance induced by the polarization of soil. Similar to the calculation of ICS in this study, the corrected imaginary part of the complex impedance was used for $Z_0''$.

### 2.4 Capacitive coupling effects in the passive setup

Four types of capacitive coupling effects need to be considered for the passive setup. As in the case of the active setup, the first type of coupling is due to the cable capacitance at the current channels. The correction method using eq. (3) can also be applied for the passive setup. After correction of the injected currents at both positive and negative current channels, the summation of the corrected currents (i.e. the leakage current $I_L$) consists of the leakage current $I_{L\_stw}$ flowing in the subsurface and back to system ground through the electrode and the wire-to-shield cable capacitance at the voltage channels (i.e. the second and third types of capacitive coupling effect) and the leakage current $I_{L\_s2s}$ through the subsurface-to-shield capacitance (i.e. the fourth type of capacitive coupling effect). The second type of capacitive coupling in the passive setup is due to the leakage current $I_{L\_w2s}$ flowing through the electrode impedance and cable capacitance at the voltage channels. Fig. 2(b) shows a circuit model for one voltage channel. The leakage current flowing through the electrode impedance $Z_e$ and the cable capacitance $C$ results in an error in the imaginary part of the measured voltage $U_m$. Similar to the correction of electrode impedance effects in laboratory SIP measurements (Huisman *et al.* 2016), the measured voltage can be corrected using

$$U_0 = U_m - i\omega C U_m Z_e \tag{6}$$

if the electrode impedance is known.

Electrode impedances can be modelled with known geometry using a complete electrode model (Rücker & Günther 2011). However, there is considerable uncertainty about the contact between the electrode and the subsurface, which typically has an unknown and heterogeneous distribution. Moreover, the small electrode size compared to the survey scale will result in a very fine mesh for the electrode model and thus a high computation load. Therefore, methods to estimate the electrode impedance from actual measurements are considered in this study. Different methods are available to estimate the electrode impedance. One method is the focus-one measurement protocol (Ingeman-Nielsen *et al.* 2016) in which the impedance of each electrode is estimated by measuring the impedance between the target electrode and all other electrodes connected in parallel. By connecting all other electrodes in parallel, the measured impedance is dominated by the impedance of the test electrode. This method is suitable when there are many electrodes so that the impedance of the parallel part of electrode becomes negligible compared to the impedance of test electrode. If the number of electrodes is low, a sequence of two-point measurements can be made. The estimated electrode impedances can be obtained through inversion of a linear system (Parsekian *et al.* 2017). In this study, two-point impedances were measured using the skip-6 circulating current injection scheme described above. The electrode impedances were then estimated by solving the following system of linear equations:

$$\begin{bmatrix} 1 & 0 & 0 & 0 & 0 & 0 & 0 & 1 & 0 & 0 & 0 \\ \vdots & & & & \ddots & & & & & \vdots \\ 1 & 0 & 0 & 0 & 1 & 0 & 0 & 0 & 0 & 0 & 0 \end{bmatrix} \begin{bmatrix} Z_{e\_01} \\ \vdots \\ Z_{e\_11} \end{bmatrix} = \begin{bmatrix} Z_{01-08} \\ \vdots \\ Z_{05-01} \end{bmatrix}, \tag{7}$$

where $Z_{e\_n}$ refers to the electrode impedance of the $n$th electrode, and $Z_{01\_08}$ represents the two-point impedance between electrode 01 and 08. To have a unique solution, the coefficient matrix must be fully ranked. For circulating measurement schemes as used in this study, the coefficient matrix is only fully ranked for an odd number of electrodes. An alternative method to estimate the electrode impedance is enabled by the design of the customized sEIT system used in this study. As shown in Fig. 2(a), the electrode impedance can be estimated using the corrected current $I$ and the voltage difference across the electrode impedance. Using the mean value of the recorded voltages at all potential electrodes to represent the voltage between electrode impedance and soil (Kelter *et al.* 2015), the impedance of the $n$th electrode can be calculated by

$$Z_{e\_n} = \frac{U_i - \text{mean}\,(U_m)}{I}. \tag{8}$$

In this study, electrode impedances estimated by inverting the two-point impedance measurements (Method-1) will be compared with the results obtained by eq. (8) (Method-2).

The third type of capacitive coupling in the passive setup is due to the leakage current $I_{L\_w2s}$ flowing in the subsurface, which creates a secondary potential field that induces an error in the imaginary part of the complex impedances. It is challenging to model this effect because of the use of a point electrode in the FEM modelling. Incorporating a complete electrode model (Rücker & Günther 2011) would allow us to consider the finite dimensions of the electrode, but the precise contact between the electrode surface and surrounding soil remains unknown. Consequently, this aspect of capacitive coupling is excluded from correction in this study, but will be discussed in relation to the fourth type of capacitive coupling and the magnitude of the measured leakage currents.

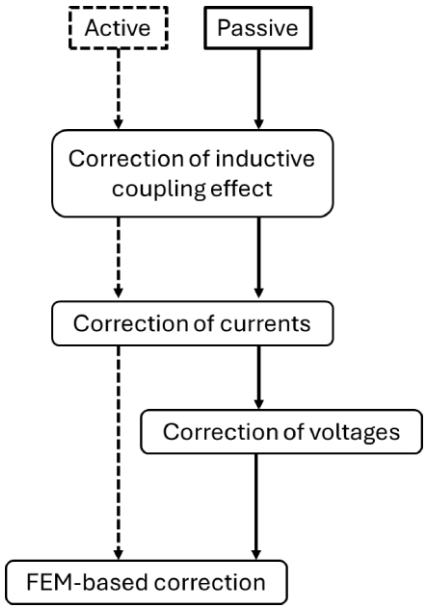


**Figure 3.** Flowchart showing the data correction procedure for active and passive setups.

The fourth type of capacitive coupling in the passive setup is the subsurface-to-shield capacitive coupling already discussed for the active setup, which can be modelled and corrected using the procedures described above. The leakage current used in the modelling is $I_{L\_s2s}$, which can be calculated by

$$I_{L\_s2s} = I_L - I_{L\_w2s}, \tag{9}$$

where the leakage current through the cable capacitances at voltage channels $I_{L\_w2s}$ is calculated using

$$I_{L\_w2s} = \sum i\omega C_n U_{m\_n}, \tag{10}$$

where $C_n$ is the cable capacitance of the $n$th cable and $U_{m\_n}$ is the measured voltage at the $n$th potential electrode.

### 2.5 Data processing workflow

Fig. 3 summarizes the data correction procedure for sEIT measurements with the active and passive set-ups. The first step of correction is the correction of inductive coupling using eq. (1), which is the same for both setups. After correction of inductive coupling, the next correction steps deal with capacitive coupling. First, a correction of the measured currents is required for both active and passive setups using eq. (3) and the model shown in Fig. 2(a). After the correction of measured currents, the next step for the passive setup is to correct the voltage error due to the electrode impedance using eq. (6) based on the model shown in Fig. 2(b). This step is not required for the active setup. The final step is the FEM-based correction to deal with the capacitive coupling between subsurface and shield of the coaxial cables. This step is necessary for both setups, but it should be noted that the leakage current required for the FEM model of the passive setup should be corrected using eqs (9) and (10).

The inversion approach of Wang *et al.* (2023) based on the FEM forward modelling engine developed by Zimmerman (2011) was used for sEIT data inversion. In particular, a two-step inversion strategy was used (Martin & Günther 2013; Wang *et al.* 2023).

In the first step, the real part of the complex impedance was inverted using the DC resistivity inversion routine. The final Jacobian matrix from the real-valued inversion is used in the second step to linearly invert for the imaginary part of the complex impedance given the Cauchy–Riemann condition for the real part of the sensitivity (Kwok 2010). The regularization parameters were determined using the approximated L-curve method (Li & Oldenburg 1999; Günther 2004) and a line search procedure was applied in each iteration to ensure stability and convergence (Günther 2004).

## 3. RESULTS AND DISCUSSION

### 3.1 Correction of measurements with the active set-up

Fig. 4 shows the sEIT measurements obtained with the active set-up. The real part of the measured impedances (Fig. 4a) ranged from 0 to 80 Ω and was slightly dependent on frequency. Figs 4(b)–(e) present the imaginary part of the impedances at different stages during the correction process. Without any correction (Fig. 4b), the imaginary part of the impedance showed substantial variation with values as high as 8 Ω at the highest frequency of 10 kHz. Positive values can also be observed in the higher frequency range. After correction of inductive coupling, only minor differences can be observed (Fig. 4c), suggesting that capacitive coupling is much stronger than inductive coupling. Two reasons can be identified for the low inductive coupling in the measurements. First, the cables are widely separated when the fan-shaped cable layout is used, resulting in small $M$ in eq. (2) compared to cables in a bundle (Wang *et al.* 2021). Secondly, the soil at this site is electrically less conductive with the real part of the apparent complex conductivity of the measurements ranged from 1.6 to 8 mS m$^{-1}$ with a mean value of 3.4 mS m$^{-1}$, resulting in larger $Z_0''$ in eq. (2). After correction of the measured currents, significant improvements were achieved (Fig. 4d). Although there still were positive values in the higher frequency range, the variation at 10 kHz decreased to 3.5 Ω. After the FEM-based correction, almost all positive values were corrected to negative values, and the variation at 10 kHz was further reduced to about 2.5 Ω (Fig. 4e). The results presented in Fig. 4(e) will be considered as the reference measurements in this study, and the measurements with the passive set-up will be compared with these reference measurements at each step of the correction.

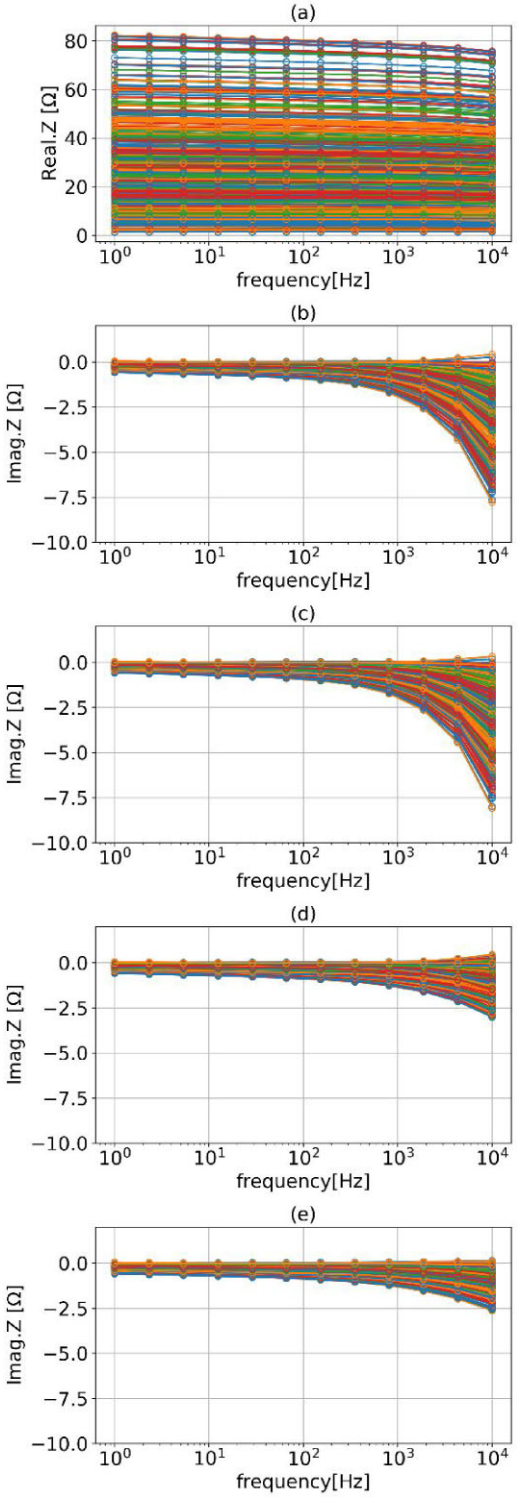


**Figure 4.** Frequency-dependent complex impedance of the sEIT measurements acquired with the active set-up: (a) the real part of the impedance, the imaginary part of the impedance (b) without any corrections, (c) after correction of inductive coupling, (d) after correction of measured currents and (e) after correction of measured currents and FEM-based correction.

### 3.2 Correction of measurements with the passive set-up

Fig. 5 shows the estimated electrode impedances using two different methods. Method-1 estimates the electrode impedances through the inversion of two-point impedance measurements, while Method-2 is enabled by the sEIT system design and calculates the electrode impedances using eq. (8). The estimated electrode impedances obtained with the two methods were similar and the differences were only minor with a maximum relative error of only 2.3 per cent. The estimated electrode impedances will be used for the correction of voltages errors using eq. (6).

Fig. 6 shows the imaginary part of the impedance obtained using the passive set-up before and after each step of correction. The real part of the impedance was almost identical with the measurements obtained with the active set-up already shown in Fig. 4(a), and therefore not presented again. Without any corrections (Fig. 6a),

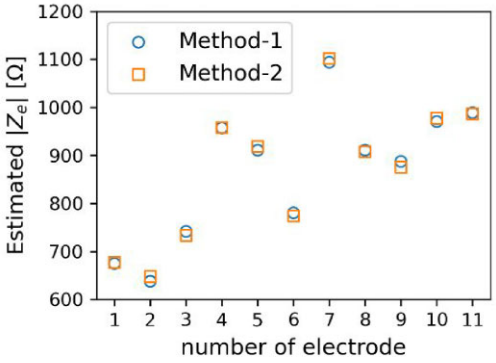


**Figure 5.** Estimated electrode impedances using Method-1: inversion of two-point impedance measurement and Method-2: system-based measurements using eq. (8).

the imaginary part of the impedance showed a large variation of about 12 Ω at the highest frequency of 10 kHz and positive values were also obtained. This larger variation for the measurements with the passive set-up compared to the variation with the active set-up (8 Ω, Fig. 4b) is expected due to the additional capacitive load at the voltage channels associated with the additional cable capacity. With the use of distributed amplifiers in the active set-up, the effect of the cable capacitances at the voltage channels is eliminated. The remaining capacitive load of the amplifier is only 5 pF in the active set-up, which is much smaller compared to the capacitive load of a 10 m coaxial cable in the passive set-up (about 1 nF for the coaxial cable type used here). After correction of inductive coupling (Fig. 6b), minor differences can be observed but the maximum variation at 10 kHz remains about 12 Ω. After correction of the measured current (Fig. 6c), the variation at 10 kHz decreased to 8 Ω. However, the observed variation is substantially higher than the variation obtained with the active set-up (3.5 Ω, Fig. 4d). After correction of the voltage errors using the estimated electrode impedances and eq. (6), the variation of the imaginary part of the impedance at 10 kHz was reduced to about 4 Ω. This is similar to the variation in the measurements with the active set-up (Fig. 4d). The final step of correction is the FEM-based correction (Fig. 6e), which further reduced the variation at 10 kHz. In contrast to the measurements with the active set-up, there are still some positive values remaining in the high frequency range after all corrections.

The effectiveness of the correction for the measurements with the passive set-up can be evaluated using the root mean square (RMS) of the differences between the reference active measurement (Fig. 4e) and the passive measurements at each correction step. It can be seen from Fig. 7 that the RMS values increased with increasing frequency due to the strong EM coupling effects at higher frequencies. The RMS values decreased significantly after the correction of the measured currents. A similar large improvement was observed after correction of the measured voltages. Further correction based on the FEM modelling also contributed to the decrease of RMS, but it is a relatively small decrease compared to the changes after correction of currents and voltages. This indicates that the cable capacitance dominates the capacitive coupling in the passive measurement set-up. The remaining error between the reference active measurements and the passive measurement after all corrections is mainly attributed to the third type of capacitive coupling in passive measurements, which was not corrected in this study for reasons outlined above.

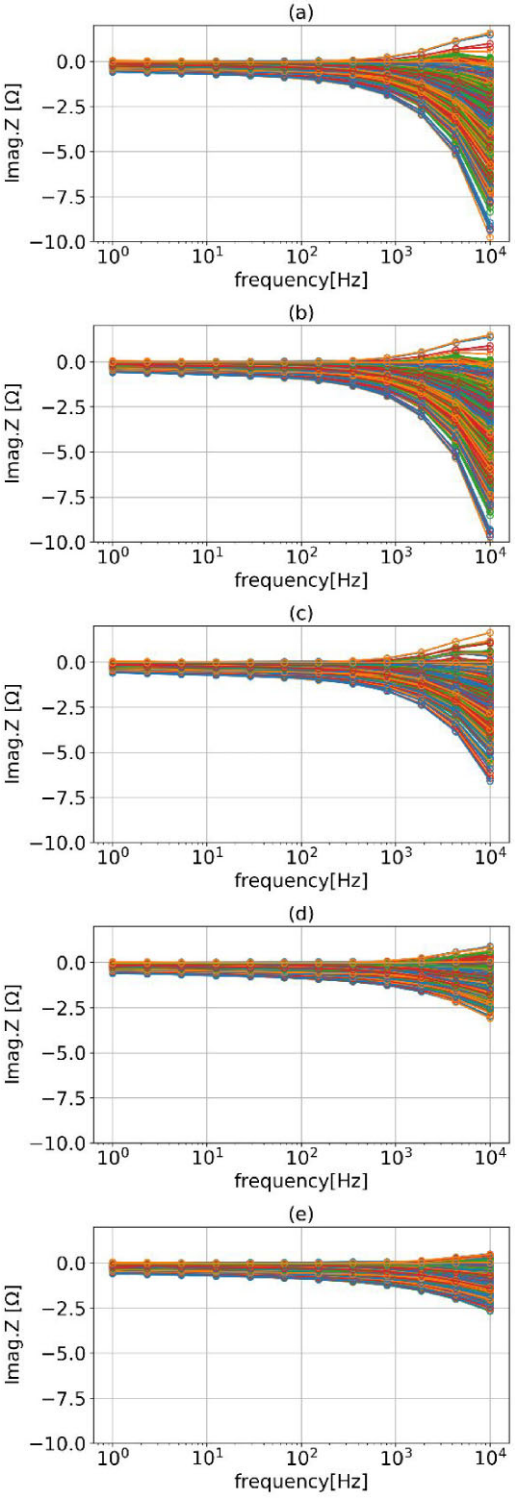


**Figure 6.** Frequency-dependent complex impedance of the sEIT measurements acquired with the passive set-up: (a) without any corrections, (b) after correction of inductive coupling, (c) after correction of measured currents, (d) after correction of measured currents and voltages and (e) after all corrections.

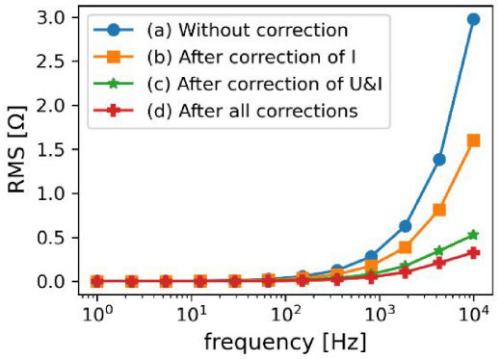


**Figure 7.** Root mean square of the differences between reference active measurements (Fig. 4e) and passive measurements after each step of correction.

### 3.3 Data filtering and inversion results

As described in Section 2.1, the first applied filter was based on the geometric factor relative error. A threshold value of 5 was applied, which resulted in 378 measurements for further processing. Figs 8(a)–(d) present the inversion results of the 378 measurements for different data sets. The inversion results for the real part of the electrical conductivity were all similar with low relative root mean square error (rRMSE). The inversion results of the imaginary part of the electrical conductivity for the reference active measurements showed good spectral consistency, and the rRMSE values were all at a low level below or around 5 per cent, indicating that the inversion results are reliable in a broad frequency range. Fig. 8(b) shows the inversion results for the passive measurements after correction of inductive coupling. Only at frequencies below 66.0 Hz, the result showed plausible inversion results that were consistent with the reference results obtained with the active set-up. At higher frequencies, the inversion results for the imaginary part of the electrical conductivity showed similar features as the results obtained for the real part of the electrical conductivity. The reason for this is that the inversion of the imaginary part of the impedance starts from a homogeneous phase model. Due to the presence of strong EM coupling in the measurements at higher frequencies, the line-search procedure gave a step length of near zero at the first iteration and the inversion stopped immediately. After correction of measured currents and voltages, the inversion results (Fig. 8c) were improved. The structure of the imaginary part of the electrical conductivity at 152.0 Hz was better captured, and the rRMSE values were reduced. After the FEM-based correction (Fig. 8d), minor improvements can

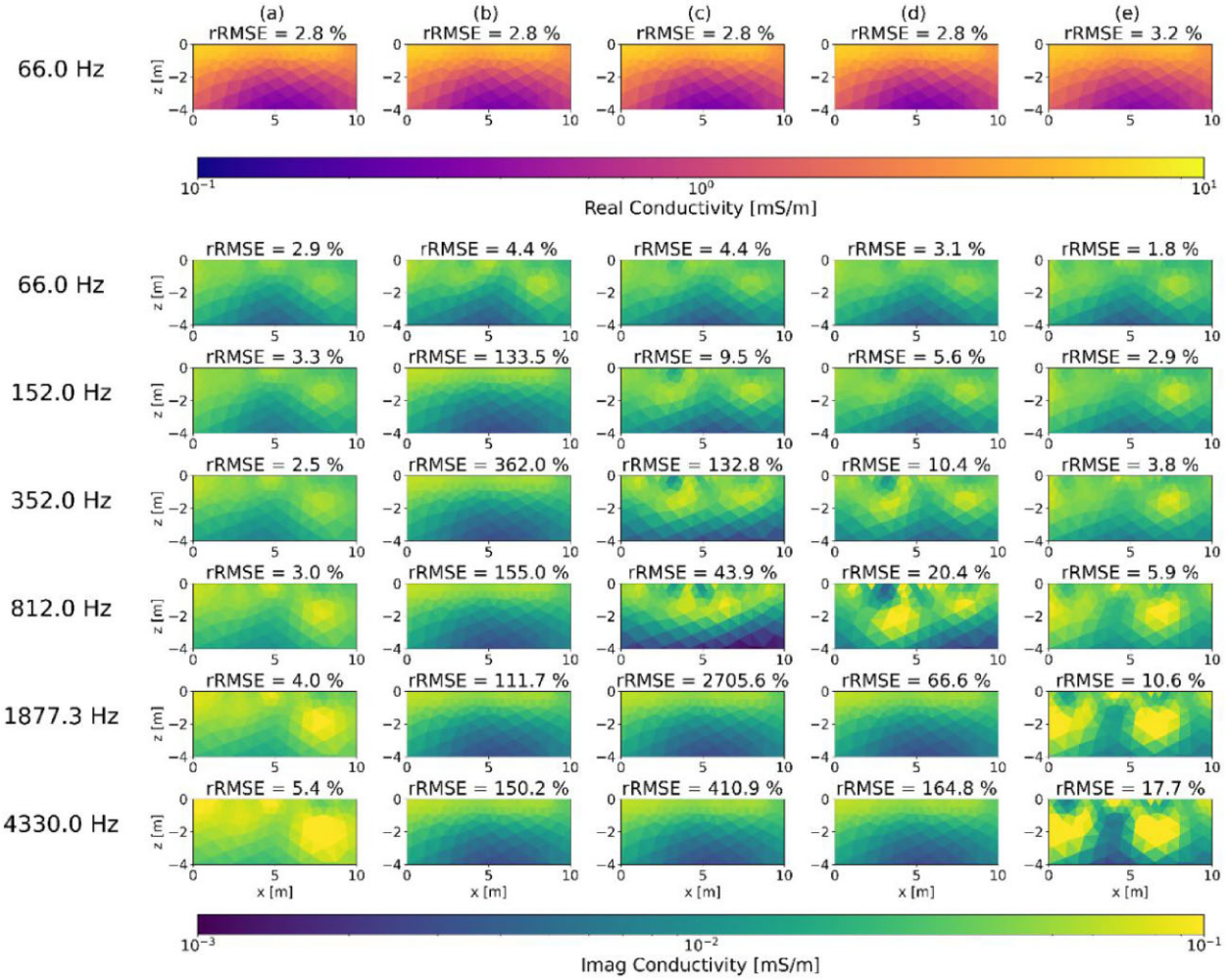


**Figure 8.** Inversion results for (a) reference active measurements, passive measurements (b) after correction of inductive coupling, (c) after correction of currents and voltages, (d) after all corrections and (e) after all corrections and filtering.

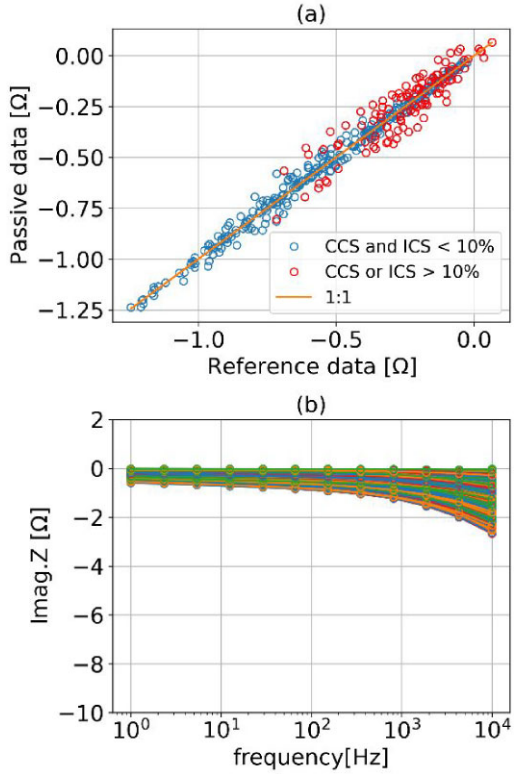


**Figure 9.** (a) Imaginary part of the impedance of the reference active measurements against the imaginary part of the impedance of the passive measurements after all corrections at 812 Hz and (b) frequency-dependent imaginary part of the impedance obtained with the passive measurement set-up after filtering based on ICS and CCS values.

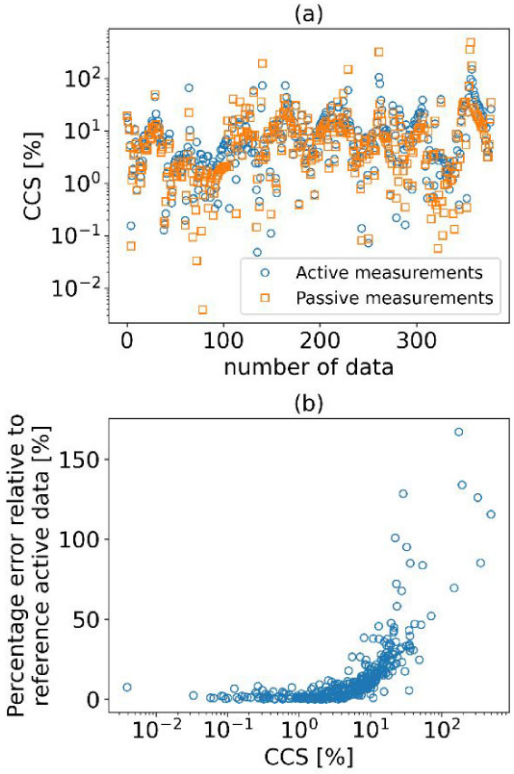


**Figure 10.** (a) CCS values of both active and passive measurements at 812 Hz and (b) CCS values of passive measurements against the percentage relative error between the corrected passive measurements (Fig. 6e) and the reference active measurements (Fig. 4e) at 812 Hz.

still be observed in the inversion results. All the rRMSE values were substantially reduced, but there were still anomalies in the inverted results.

To further improve the results at 352.0 and 812.0 Hz, the ICS and CCS values at 812.0 Hz were examined. Most of the measurements have ICS values below 5 per cent and only 10 out of the 378 measurements have ICS values larger than 10 per cent. For the CCS values, 106 out of 378 measurements have CCS values larger than 10 per cent. Fig. 9(a) shows a scatter plot of the imaginary part of the impedance of the reference active measurements against the passive measurements after all corrections. Measurements with an ICS or CCS larger than 10 per cent attributed considerably to the observed scatter. Using a 10 per cent threshold value for both CCS and ICS for data filtering, 271 data points remained. The imaginary part of the impedance after filtering (Fig. 9b) does not show positive values anymore. The improvement in data quality was also observed from the inversion results (Fig. 8e). After data filtering, the inversion results at 352.0 and 812.0 Hz were largely improved and showed more similarity with the inversion results of the reference active measurements. The inversion results at higher frequencies were also improved, as indicated by the strongly reduced rRMSE values. However, some differences can still be observed compared to the results of the reference active measurements. Overall, it was concluded that broad-band sEIT imaging results can be achieved by measurements with a centralized multiplexer and coaxial cables after applying the novel data correction approach and the previously established filtering based on ICS and CCS values.

It should be noted that data filtering was only applied to the measurements with the passive set-up. For the active set-up, consistent broad-band inversion results were already achieved after correction of the measurements only, as shown in Fig. 8. However, the measurements with the active and passive set-up have comparable CCS values, as shown in Fig. 10(a). The CCS values are mostly below 100 per cent with mean values of 11.6 per cent and 12.7 per cent for the active and passive set-up, respectively. Fig. 10(b) shows the CCS values for the measurements with the passive set-up at 812 Hz against the individual relative error between the measurements with the active and passive set-up. It can be observed that high CCS values correspond to high relative errors between the active and passive set-up. Particularly, the relative error increases significantly when CCS is above 10 per cent. This indicates that the CCS values also reflect the strength of the third type of capacitive coupling, which could not be corrected here. Therefore, data filtering based on CCS improved the inversion results of passive measurements.

## 4. CONCLUSIONS AND OUTLOOK

In this study, EM coupling effects in broad-band sEIT measurements acquired using a centralized multiplexer and coaxial cables (passive setup) were investigated. The measurements with the passive set-up were compared to sEIT measurements obtained using distributed amplifiers (active setup). To enable measurements with the same sEIT instrument for both setups, a connector hub was developed that functions as the centralized multiplexer, thus extending the capabilities of the system initially designed for use

with distributed amplifiers. This advancement is particularly advantageous for borehole sEIT measurements, where amplifier modules placed at the electrodes are susceptible to breakdown in case of water leakage. By utilizing the connector hub and the correction methods developed in this work, accurate broad-band borehole sEIT measurements with the customized EIT40 system can be acquired without risk of damaging the electronic components at the electrodes.

In a next step, EM coupling effects were analysed for the active and passive setups. Following the methods proposed in previous work, the measurements with the active set-up were corrected, and the final corrected data set was considered as the reference to evaluate the corrections of the measurement with the passive set-up. For the passive setup, four correction steps were required. As for the active measurements, the first and second step are the correction of inductive coupling and the measured currents, respectively. The third step involved correcting voltage errors due to the cable capacitance at the potential measurement channels, which required knowledge of both electrode impedances and cable capacitances. Two methods for estimating electrode impedance were compared, showing high agreement between the results. The final correction step, similar to the active setup, was based on FEM modeling, but the leakage currents should be corrected before implementation in the modelling. After each correction step, the measurements with the passive set-up were compared to the reference measurements with the active set-up. The RMS values between the two sets of measurements demonstrated the effectiveness of the corrections. It was observed that the cable capacitance dominates the capacitive coupling in the passive measurement set-up, while the capacitive coupling between the subsurface and the cable shield became secondary although it still needs to be considered to achieve accurate broad-band measurement results. Improvements were also evident in the inversion results. Reliable inversion results were achieved up to the kHz range, following additional data filtering using ICS and CCS. It was concluded that broad-band sEIT imaging can be achieved with a centralized multiplexer and coaxial cables by applying appropriate correction and filtering methods.

While this study demonstrated promising sEIT results using a centralized multiplexer, the presented methods for correction of the capacitive coupling effects still rely largely on the design of the custom-made EIT40 system. Further testing with commercially available systems that are specifically designed for centralized multiplexers is necessary. However, several considerations must be taken into account for these systems when designing the measurement strategies. First, both positive and negative channel currents need to be measured for current correction, whereas commercial systems typically only measure the current through a single reference resistor at one current channel in the system. To achieve this with other systems, shunt resistors should be implemented at both the positive and negative current channels and voltages on the two shunt resistors should be measured to calculate the currents at both channels. Secondly, voltage correction requires measurements relative to the cable shield (system ground) instead of the voltage difference between two electrodes commonly measured by commercially available systems. This issue could be resolved by connecting all shields to a common point, such as the system ground as in the EIT40 system used in this study or a single electrode placed far away from the system (Flores Orozco *et al.* 2021), after which the voltages could be measured relative to this reference electrode.

Finally, a detailed investigation of EM coupling effects when using non-shielded wires with a centralized multiplexer is also warranted. Time-domain induced polarization (TDIP) surveys, which are commonly conducted in the field, are usually carried out with non-shielded wires in a cable bundle and systems with a centralized multiplexer. A previous study expanded the bandwidth of TDIP measurements through advanced signal processing techniques (Olsson *et al.* 2016). However, EM coupling effects have not yet been accounted for in TDIP measurements, although it was recognized that the small distance between the wires in the cable bundle induced strong EM coupling effects. Key questions are whether separating the wires can improve TDIP measurements at early times and whether careful measurement design can mitigate EM coupling effects in TDIP measurements. Addressing these questions is crucial for further enhancing the bandwidth of TDIP measurements.

## ACKNOWLEDGMENTS

The authors would like to thank Tarig Bukhary, Odilia Esser, Salar Saeed Dogar and Walter Glaas for help with the equipment and field measurements. We also thank the two reviewers, Dr Youzheng Qi and Dr Alex Furman, and the editor Dr Line Madsen, for their constructive feedback.

## DATA AVAILABILITY

The data supporting the findings of this study are available upon reasonable request.

## REFERENCES

Aal, G.Z.A. & Atekwana, E.A., 2014. Spectral induced polarization (SIP) response of biodegraded oil in porous media, *Geophys. J. Int.,* **196,** 804–817.

Attwa, M. & Günther, T., 2013. Spectral induced polarization measurements for predicting the hydraulic conductivity in sandy aquifers, *Hydrol. Earth Syst. Sci.,* **17,** 4079–4094.

Carpenter, E. & Habberjam, G., 1956. A tri-potential method of resistivity prospecting, *Geophysics,***21,** 455–469.

Commer, M., Newman, G.A., Williams, K.H. & Hubbard, S.S., 2011. 3D induced-polarization data inversion for complex resistivity, *Geophysics,***76,** F157–F171.

Dahlin, T. & Leroux, V., 2012. Improvement in time-domain induced polarization data quality with multi-electrode systems by separating current and potential cables, *Surf. Geophys.,* **10,** 545–565.

Flores Orozco, A., Aigner, L. & Gallistl, J., 2021. Investigation of cable effects in spectral induced polarization imaging at the field scale using multicore and coaxial cables, *Geophysics,***86,** E59–E75.

Flores Orozco, A., Williams, K.H., Long, P.E., Hubbard, S.S. & Kemna, A., 2011. Using complex resistivity imaging to infer biogeochemical processes associated with bioremediation of an uranium-contaminated aquifer, *J. Geophys. Res.-Biogeosciences.,* **116**.

Flores Orozco, A.., Kemna, A., Oberdoerster, C., Zschornack, L., Leven, C., Dietrich, P. & Weiss, H., 2012. Delineation of subsurface hydrocarbon contamination at a former hydrogenation plant using spectral induced polarization imaging, *J. Contam. Hydrol.,* **136-137,** 131–144.

Günther, T., 2004. *Inversion Methods and Resolution Analysis for the 2D/3D Reconstruction of Resistivity Structures from DC Measurements, Thesis*.

Huisman, J.A., Zimmermann, E., Esser, O., Haegel, F.H., Treichel, A. & Vereecken, H., 2016. Evaluation of a novel correction procedure to remove electrode impedance effects from broadband SIP measurements, *J. Appl. Geophys.,* **135,** 466–473.

Ingeman-Nielsen, T., Tomaškovičová, S. & Dahlin, T., 2016. Effect of electrode shape on grounding resistances—Part 1: the focus-one protocol, *Geophysics,* **81,** WA159–WA167.

Izumoto, S., Huisman, J.A., Wu, Y. & Vereecken, H., 2020. Effect of solute concentration on the spectral induced polarization response of calcite precipitation, *Geophys. J. Int.,* **220,** 1187–1196.

Kelter, M., Huisman, J.A., Zimmermann, E., Kemna, A. & Vereecken, H., 2015. Quantitative imaging of spectral electrical properties of variably saturated soil columns, *J. Appl. Geophys.,* **123,** 333–344.

Kwok, Y.K., 2010. *Applied Complex Variables for Scientists and Engineers,* Cambridge Univ. Press.

Li, Y. & Oldenburg, D.W., 1999. 3-D inversion of DC resistivity data using an L-curve criterion, *SEG Tech. Program Expand. Abstr. 1999,* Society of Exploration Geophysicists.

Loke, M.H., Wilkinson, P.B., Uhlemann, S.S., Chambers, J.E. & Oxby, L.S., 2014. Computation of optimized arrays for 3-D electrical imaging surveys, *Geophys. J. Int.,* **199,** 1751–1764.

Martin, T. & Günther, T., 2013. Complex resistivity tomography (CRT) for fungus detection on standing oak trees, *Eur. J. Res.,* **132,** 765–776.

Mellage, A., Smeaton, C.M., Furman, A., Atekwana, E.A., Rezanezhad, F. & Van Cappellen, P., 2018. Linking spectral induced polarization (SIP) and subsurface microbial processes: results from sand column incubation experiments, *Environ. Sci. Technol.,* **52,** 2081–2090.

Olsson, P.-I., Fiandaca, G., Larsen, J.J., Dahlin, T. & Auken, E., 2016. Doubling the spectrum of time-domain induced polarization by harmonic de-noising, drift correction, spike removal, tapered gating and data uncertainty estimation, *Geophys. Suppl. Mon. Not. R. Astron. Soc.,* **207,** 774–784. The Royal Astronomical Society.

Parsekian, A.D. *et al.*, 2017. Comparing measurement response and inverted results of electrical resistivity tomography instruments, *J. Environ. Eng. Geophys.,* **22,** 249–266.

Personna, Y.R., Ntarlagiannis, D., Slater, L., Yee, N., O'Brien, M. & Hubbard, S., 2008. Spectral induced polarization and electrodic potential monitoring of microbially mediated iron sulfide transformations, *J. Geophys. Res. Biogeosciences,* **113,** John Wiley & Sons, Ltd.

Qi, Y., El-Kaliouby, H., Revil, A., Ahmed, A.S., Ghorbani, A. & Li, J., 2019. Three-dimensional modeling of frequency-and time-domain electromagnetic methods with induced polarization effects, *Comput. Geosci.,* **124,** 85–92. Elsevier.

Routh, P.S. & Oldenburg, D.W., 2001. Electromagnetic coupling in frequency-domain induced polarization data: a method for removal, *Geophys. J. Int.,* **145,** 59–76.

Rücker, C. & Günther, T., 2011. The simulation of finite ERT electrodes using the complete electrode model, *Geophysics,* **76,** F227–F238. Society of Exploration Geophysicists.

Schmutz, M., Ghorbani, A., Vaudelet, P. & Blondel, A., 2014. Cable arrangement to reduce electromagnetic coupling effects in spectral-induced polarization studies, *Geophysics,***79,** A1–A5.

Schulz, R., Burger, I., Pischke, A., Westermann, S. & Hördt, A., 2025. *Ice Content Estimation in a Palsa at Aidejavri (Norway) Using High-Frequency Induced Polarization (HFIP),* Copernicus GmbH.

Sunde, E.D., 1968. *Earth Conduction Effects in Transmission Systems,* Dover Publications Inc.

Wait, J.R., 1984. Electromagnetic response of a discretely grounded circuit, *Geophysics,* **49,** 577–580.

Wait, J.R. & Gruszka, T.P., 1986. On electromagnetic coupling removal from induced polarization surveys, *Geoexploration,***24,** 21–27.

Wang, H., Huisman, J.A., Zimmermann, E. & Vereecken, H., 2021. Experimental design to reduce inductive coupling in spectral electrical impedance tomography (sEIT) measurements, *Geophys. J. Int.*. **225,** 222–235.

Wang, H., Huisman, J.A., Zimmermann, E. & Vereecken, H., 2024. Tackling capacitive coupling in broad-band spectral electrical impedance tomography (sEIT) measurements by selecting electrode configurations, *Geophys. J. Int.,* **238,** 187–198.

Wang, H., Zimmermann, E., Weigand, M., Vereecken, H. & Huisman, J.A., 2023. Comparison of different inversion strategies for electrical impedance tomography (EIT) measurements, *Geophys. J. Int.,* **235,** 2888–2899. Oxford University Press.

Weigand, M., Zimmermann, E., Michels, V., Huisman, J.A. & Kemna, A., 2022. Design and operation of a long-term monitoring system for spectral electrical impedance tomography (sEIT), *Geosci. Instrum. Method Data Syst. Discuss.,* **11,** 413–433.

Wilkinson, P.B., Chambers, J.E., Lelliott, M., Wealthall, G.P. & Ogilvy, R.D., 2008. Extreme sensitivity of crosshole electrical resistivity tomography measurements to geometric errors, *Geophys. J. Int.,* **173,** 49–62.

Williams, K.H. *et al.*, 2009. Geophysical monitoring of coupled microbial and geochemical processes during stimulated subsurface bioremediation, *Environ. Sci. Technol.,* **43,** 6717–6723.

Xu, B.W. & Noel, M., 1993. On the completeness of data sets with multi-electrode systems for electrical resistivity survey, *Geophys. Prospect.,* **41,** 791–801.

Zhao, Y., Zimmermann, E., Huisman, J.A., Treichel, A., Wolters, B., Waasen, S.v. & Kemna, A., 2013. Broadband EIT borehole measurements with high phase accuracy using numerical corrections of electromagnetic coupling effects, *Meas. Sci. Technol.,* **24,** 085005.

Zhao, Y., Zimmermann, E., Huisman, J.A., Treichel, A., Wolters, B., Waasen, S.v. & Kemna, A., 2015. Phase correction of electromagnetic coupling effects in cross-borehole EIT measurements, *Meas. Sci. Technol.,* **26,** 015801.

Zimmermann, E., 2011. *Phasengenaue Impedanzspektroskopie und -tomographie für Geophysikalische Anwendungen, Thesis*.

Zimmermann, E. *et al.*, 2010. Advanced electrical impedance tomography system with high phase accuracy, in *Proc. 6th World Congr. Ind. Process Tomogr. WCIPT6,* Beijing, China, pp. 583–591.

Zimmermann, E., Huisman, J.A., Mester, A. & Waasen, S.v., 2019. Correction of phase errors due to leakage currents in wideband EIT field measurements on soil and sediments, *Meas. Sci. Technol.,* **30,** 084002.

Zimmermann, E., Kemna, A., Berwix, J., Glaas, W. & Vereecken, H., 2008. EIT measurement system with high phase accuracy for the imaging of spectral induced polarization properties of soils and sediments, *Meas. Sci. Technol.,* **19,** 094010.